


Cite this: *RSC Adv.*, 2018, 8, 28538

Synthesis and photoluminescence properties of novel far-red-emitting BaLaMgNbO₆:Mn⁴⁺ phosphors for plant growth LEDs

Qi Sun, Shaoying Wang, Balaji Devakumar, Bin Li, Liangling Sun, Jia Liang and Xiaoyong Huang *

A series of far-red-emitting BaLaMgNbO₆:Mn⁴⁺ (BLMN:Mn⁴⁺) phosphors were successfully synthesized by a high-temperature solid-state reaction method. Crystal structure and luminescence properties of the obtained samples were systematically investigated. The emission spectra exhibited a strong narrow far-red emission band peaking at 700 nm with a full width at half-maximum (FWHM) of ~36 nm under 360 nm excitation. The optimal Mn⁴⁺ concentration was about 0.4 mol%. The internal quantum efficiency and CIE chromaticity coordinates of the BLMN:0.4% Mn⁴⁺ phosphor were 52% and (0.7222, 0.2777), respectively. In addition, the luminescence mechanism has been analyzed using a Tanabe–Sugano energy level diagram. Finally, by using a 365 nm near-ultraviolet InGaN chip combined with BLMN:0.4% Mn⁴⁺ phosphors, a far-red LED device was fabricated.

Received 16th July 2018
Accepted 3rd August 2018

DOI: 10.1039/c8ra06048g

rsc.li/rsc-advances

Introduction

Light plays a key role in indoor plant cultivation, especially for plants that have a high demand for light.^{1,2} It is known that light controls the process of plant growth, because blue light around 450 nm (410–500 nm) promotes leaf growth, stomatal opening, and photosynthesis, and red light around 660 nm (610–700 nm) contributes to the growth of plant stems and phototropism, while far-red light around 730 nm (700–740 nm) modulates the process of plant germination and plant flowering time.^{3–6} Phytochrome regulates plant growth and development, which have two types – P_R and P_{FR}, P_R absorbs red light peaked at 660 nm and P_{FR} absorbs far-red light centered at about 730 nm.^{7,8} Compared to traditional incandescent and fluorescent lamps, light emitting diodes (LEDs) have become the promising candidates for artificial light sources for plant growth due to their extraordinary advantages such as the high luminescence efficiency, energy saving, and good stability.^{9–18} Especially, LEDs can adjust the spectral composition by using various phosphors to match with the spectrum of plant photosynthesis and photomorphogenesis. So, nowadays LEDs have been widely applied in indoor plant growth.¹⁹

In recent years, non-rare-earth Mn⁴⁺ doped red-emitting phosphors for LEDs for plant growth have attracted tremendous attention, because the price for the rare-earth materials has been increasing sharply due to the shortage in the supply of rare-earth materials.^{20,21} It is well known that Mn⁴⁺ ion with the

d³ electron configuration can emit red or far red luminescence with emission wavelengths ranging from 600 to 800 nm under ultraviolet (UV)/blue excitation, resulting from its ²E_g → ⁴A_{2g} transition in a strong crystal field.^{22–25} Recently, Mn⁴⁺-activated red phosphors have been extensively studied.²⁶ Mn⁴⁺ doped fluorides show intense excitation band located at ~460 nm and sharp red emission centered at ~630 nm.^{27–30} Unfortunately, the toxic HF solution used in preparation process is harmful to the environment and humans, and these fluorides have poor stability in moisture environment. As an alternative, Mn⁴⁺ doped oxides, such as Li₂MgTiO₄:Mn⁴⁺, Li₂MgZrO₄:Mn⁴⁺, and Ba₂YNbO₆:Mn⁴⁺ give rise to far-red emissions and have eco-friendly preparation process, which thus can be considered as potential red-emitting phosphors for LEDs.^{5,23,31,32} Thus, searching for appropriate hosts providing abundant octahedral sites for Mn⁴⁺ ions is urgent.

Compounds with perovskite structure are regarded as potential hosts owing to their good chemical stability and superior optical properties.^{33–40} Among the oxides, many niobate-based perovskite-structured phosphors, such as Ca₂GdNbO₆:Mn⁴⁺, Ba₂YNbO₆:Mn⁴⁺, Ba₂GdNbO₆:Mn⁴⁺, and Sr₂LaNbO₆:Mn⁴⁺, have attracted considerable attention.^{31,41–43} BaLaMgNbO₆ (BLMN) has many [NbO₆] octahedrons with a cubic crystal structure that are suitable for Mn⁴⁺ doping. In this present paper, we reported novel double-perovskite BLMN:Mn⁴⁺ far-red-emitting phosphors, which have been synthesized through high-temperature solid-state reaction in air. It was found that under 360 nm excitation, BLMN:Mn⁴⁺ phosphors showed an intense emission band centered at 700 nm between 650 and 800 nm, which was matched well with the absorption band of phytochrome P_{FR}. The optimal doping

Key Lab of Advanced Transducers and Intelligent Control System, Ministry of Education and Shanxi Province, College of Physics and Optoelectronics, Taiyuan University of Technology, Taiyuan 030024, PR China. E-mail: huangxy04@126.com



concentration of Mn^{4+} was about 0.4 mol%. The CIE chromaticity coordinates and internal quantum efficiency (IQE) of BLMN:0.4% Mn^{4+} sample were (0.7222, 0.2777) and 52%, respectively. Moreover, the concentration quenching mechanism was discussed. In addition, the luminescence mechanism was explained by the Tanabe–Sugano energy level diagram. Thermal quenching characteristics were also analyzed. All these investigations demonstrated that BLMN: Mn^{4+} phosphors are promising far-red-emitting materials for far-red LEDs for plant growth.

Experimental

A series of $\text{BaLaMgNb}_{1-x}\text{O}_6:\text{xMn}^{4+}$ (BLMN: xMn^{4+} ; $x = 0.05\%$, 0.1%, 0.2%, 0.4%, 0.8%, and 1.0%) phosphors were successfully synthesized through a high-temperature solid-state reaction method. BaCO_3 (analytical reagent, AR), La_2O_3 (99.99%), MgO (AR), Nb_2O_5 (AR), and MnCO_3 (AR) were used as the raw materials. According to the stoichiometric ratio, these raw materials were weighted and ground in an agate mortar to achieve uniformity. The obtained mixtures were transferred to the alumina crucibles and pre-calcined at 500 °C for 3 h, then sintered at 1500 °C for 6 h in air. Finally, the samples were cooled to room temperature naturally in the furnace, and they were reground again to obtain final samples for further characterizations.

The X-ray diffraction (XRD) patterns of the samples were recorded on a Bruker D8 X-ray diffractometer using $\text{Cu K}\alpha$ radiation. The morphology properties of the samples were analyzed by using a field-emission scanning electron microscope (FE-SEM; TESCAN MAIA3). The photoluminescence (PL) and PL excitation (PLE) spectra and decay lifetimes were measured by an Edinburgh FS5 spectrometer equipped with a 150 W continued-wavelength xenon lamp and a pulsed xenon lamp, respectively. The IQE was measured by an Edinburgh FS5 spectrometer equipped with an integrating sphere coated with BaSO_4 .

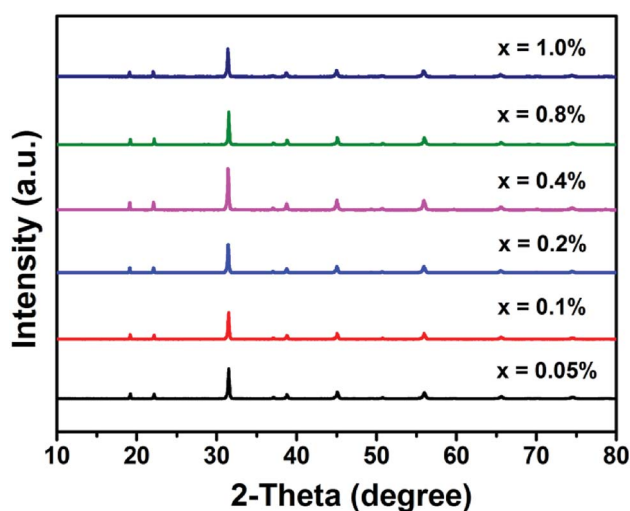


Fig. 1 XRD patterns of BLMN: xMn^{4+} ($x = 0.05\%$, 0.1%, 0.2%, 0.4%, 0.8%, and 1.0%) phosphors.

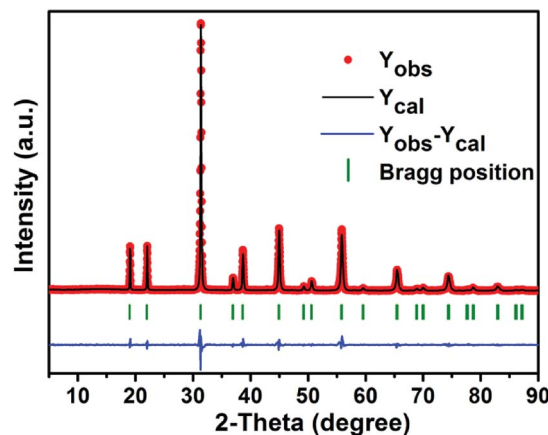


Fig. 2 Rietveld refinement XRD patterns of BLMN:0.4% Mn^{4+} phosphors.

Results and discussion

Fig. 1 shows the XRD patterns of the as-prepared BLMN: xMn^{4+} ($x = 0.05\%$, 0.1%, 0.2%, 0.4%, 0.8%, and 1.0%) samples. It can be seen that all the samples exhibited similar diffraction patterns, indicating that increasing Mn^{4+} ions concentration does not significantly influence the crystal structure.

To further analyze the crystal structure details of the as-prepared samples, Rietveld refinement of BLMN:0.4% Mn^{4+} was carried out. The refined results for the XRD profile of BLMN:0.4% Mn^{4+} are shown in Fig. 2, including the observed (dot), calculated patterns (black line), the difference between the experimental and calculated data (blue line), and the positions of Bragg reflection (short vertical green line). The final refinement data R_{wp} and R_p were determined to be 10.84% and 8.93%, respectively, indicating the refined results were reliable. The final refined crystallographic data were listed in Table 1.

Fig. 3 presents the crystal structure of BLMN:0.4% Mn^{4+} . The BLMN:0.4% Mn^{4+} belongs to double-perovskite oxide and has a cubic system with space group $Fm\bar{3}m$. The lattice parameters are $a = b = c = 8.0620 \text{ \AA}$, $V = 523.99 \text{ \AA}^3$, $N = 4$ and $\alpha = \beta = \gamma = 90^\circ$. It can be found that Nb^{5+} and Mg^{2+} ions occupy octahedral sites with six oxygen atoms surrounded. BLMN has many $[\text{NbO}_6]$ octahedral sites, which are suitable for Mn^{4+} ions doping. Mn^{4+} ions prefer to substitute for the Nb^{5+} ions over Mg^{2+} , Ba^{2+} and La^{3+} ions owing to the similar ionic radii (0.53 Å for Mn^{4+} , 0.64 Å for Nb^{5+} , 0.72 Å for Mg^{2+} , 1.35 Å for Ba^{2+} and 1.32 Å for La^{3+}).⁴⁴ As well-known, the radius percentage

Table 1 Refined structural data of BLMN:0.4% Mn^{4+} sample

Formula	BLMN:0.4% Mn^{4+}
Crystal system	Cubic
Space group	$Fm\bar{3}m$
$a = b = c$	8.0620 Å
$\alpha = \beta = \gamma$	90°
V	523.99 Å ³
N	4
R_{wp}	10.84%
R_p	8.93%



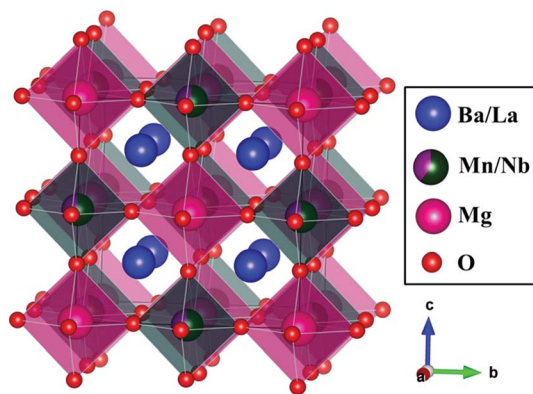


Fig. 3 The crystal structure of BLMN:0.4% Mn⁴⁺.

difference between the doped ions and the substituted ions should be less than 30%. The radius percentage difference between Mn⁴⁺ ions and Nb⁵⁺ ions can be estimated using the following equation:³⁴

$$D_r = \frac{R_s(\text{CN}) - R_d(\text{CN})}{R_s(\text{CN})} \times 100\% \quad (1)$$

where D_r is the difference in radius percentage, $R_s(\text{CN})$ and $R_d(\text{CN})$ are the radius of the host ions and doped ions with different coordination number CN, respectively. The calculated D_r was determined to be around 17%, which was much smaller than 30%. Therefore, the Mn⁴⁺ ions were substitute for Nb⁵⁺ ions in the BLMN host lattice.

Fig. 4(a and b) shows the SEM images of the as-prepared BLMN:0.4% Mn⁴⁺ sample. It can be clearly seen that the obtain sample was agglomerated and the particle size ranged within 1–4 μm. Moreover, the corresponding element mapping results were shown in Fig. 4(c–h). The components of Ba, La, Mg, Nb, O, Mn elements were uniformly distributed on the surface of particles. The results further proved that the Mn⁴⁺ ions were well-doped in the BLMN host.⁴⁵

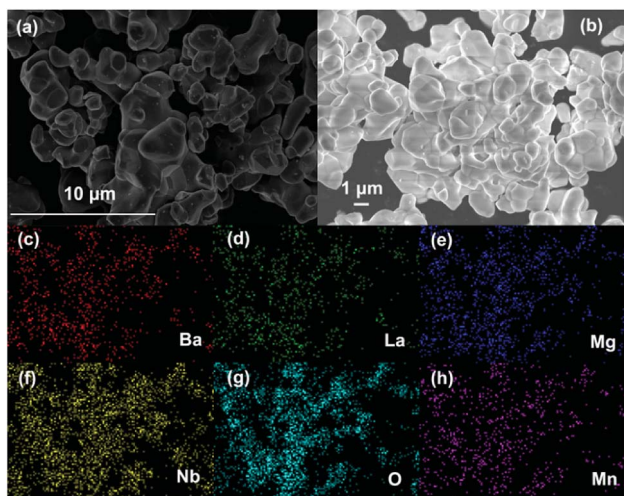


Fig. 4 FE-SEM images (a and b) and elements mapping images (c–h).

Fig. 5(a) shows the typical PLE and PL spectra of BLMN:0.4% Mn⁴⁺ sample. When monitored at 700 nm, the PLE spectrum exhibited two broad excitation bands in the region of 250 to 600 nm, which could be fitted by four Gaussian curves. The four deconvoluted Gaussian peaks centered at 327, 375, 472, and 520 nm could be ascribed to Mn–O charge transfer band (CTB), and the Mn⁴⁺ spin-allowed transitions of $^4A_{2g} \rightarrow ^4T_{1g}$, $^4A_{2g} \rightarrow ^2T_{2g}$, and $^4A_{2g} \rightarrow ^4T_{2g}$, respectively.⁴⁶ The PLE spectrum indicated that the BLMN:Mn⁴⁺ phosphors can be efficiently excited by near-UV or blue LED chips. When excited at 360 nm and 469 nm, the BLMN:Mn⁴⁺ phosphors showed an intense far red emission peaking at 700 nm in the wavelength range of 650–800 nm, which was attributed to $^2E_g \rightarrow ^4A_{2g}$ transition of Mn⁴⁺ ions in the $[\text{MnO}_6]^{8-}$ octahedral environment.^{47–50} Moreover, the full-width at half maximum (FWHM) was as narrow as ~36 nm. Fig. 5(b) shows PL spectrum of BLMN:0.4% Mn⁴⁺ phosphors and the absorption spectrum of phytochrome P_{FR}. An obvious overlap between the absorption spectrum of phytochrome P_{FR} and the emissions spectrum of BLMN:0.4% Mn⁴⁺ phosphors was observed, which suggested the BLMN:Mn⁴⁺ phosphors could be used as far-red emitting materials for plant growth LEDs. Fig. 5(c) shows the PL spectra of BLMN:Mn⁴⁺ phosphors with different Mn⁴⁺ doping concentrations under 360 nm excitation. There was no change in peak shape and position with increasing Mn⁴⁺ concentration except for the emission intensity. It can be clearly seen that the PL emission intensity increased gradually with increasing the doping concentration until it reached a maximum at $x = 0.4\%$, then began to decrease with further increasing Mn⁴⁺ content owing to the concentration quenching effect.^{51–53} With increasing the doping concentration, the distance between Mn⁴⁺–Mn⁴⁺ ions decreased, the possibility of energy transfer between the nearest Mn⁴⁺ ions increased, leading to lower the luminescence efficiency. In the BLMN:Mn⁴⁺ phosphors the energy transfer mechanism can not be the radiation reabsorption, because there is no overlap between PLE and PL spectra of Mn⁴⁺ ions.²² It might be related to exchange interaction or electric multipolar interaction. The critical distance (R_c) was roughly estimated by the following formula:⁵⁴

$$R_c = 2 \left[\frac{3V}{4\pi CN} \right]^{1/3} \quad (2)$$

where V is the volume of the unit cell, C is the critical doped concentration of Mn⁴⁺, and N is the number of dopant sites available per unit cell. In the BLMN:0.4% Mn⁴⁺ case, the $C = 0.4\%$; $V = 523.99 \text{ \AA}^3$; $N = 4$. Thus, R_c was calculated to be about 39.69 Å. Because the exchange interaction is possible only when the R_c is smaller than 5 Å, so the electric multipolar interaction was the major mechanism of the energy transfer between Mn⁴⁺ ions in BLMN host. Furthermore, the detailed concentration quenching mechanism can be analyzed by the following equation:⁵⁵

$$\log(I/x) = A - (\theta/3)\log x \quad (3)$$

where I is the emission intensity, x is the activator ion concentration, A is concentration and the values of $\theta = 6, 8$ and



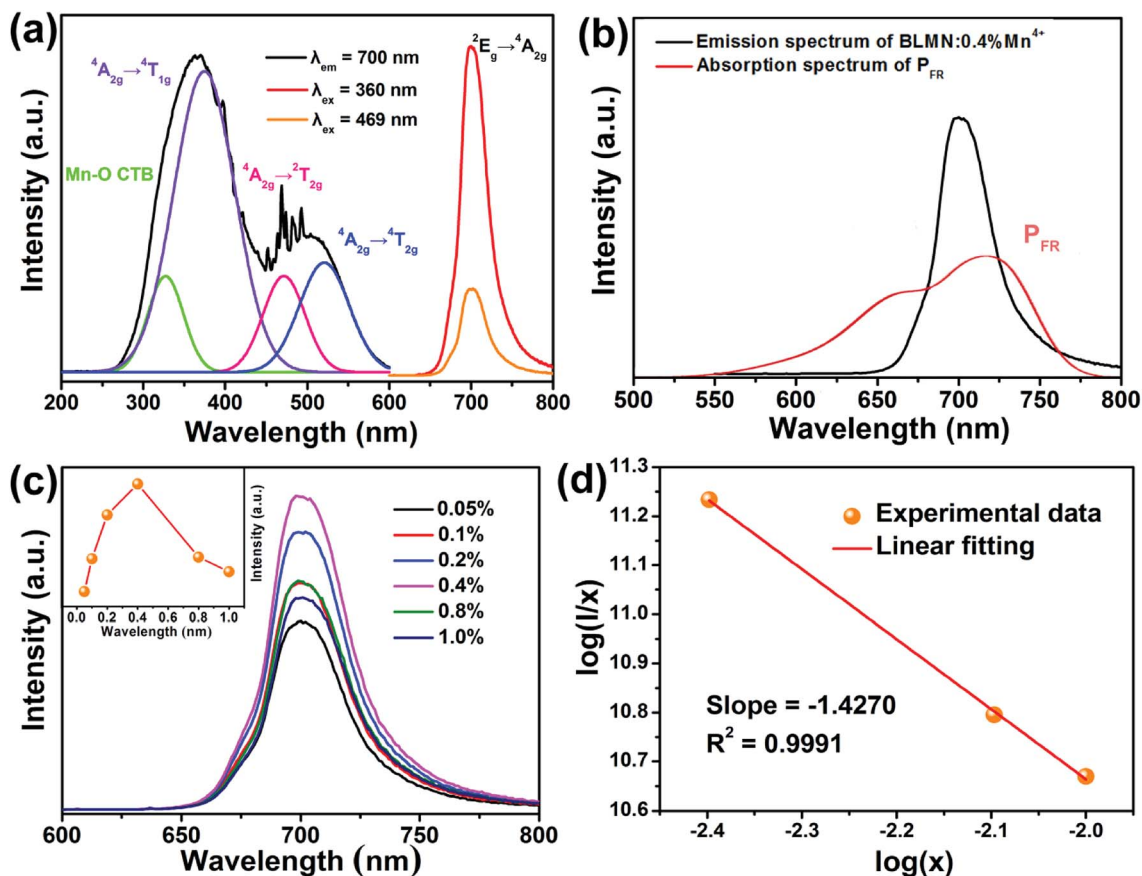


Fig. 5 (a) PLE and PL spectra of BLMN:0.4% Mn⁴⁺ sample. (b) PL spectrum of BLMN:0.4% Mn⁴⁺ phosphors and the absorption spectra of phytochrome P_{FR}. (c) PL spectra of BLMN:xMn⁴⁺ (x = 0.05%, 0.1%, 0.2%, 0.4%, 0.8%, and 1.0%) phosphors under 360 nm excitation. The inset shows the integrated emission intensity of BLMN:xMn⁴⁺ as a function of Mn⁴⁺ concentrations. (d) The dependence of log(I/x) on log(x) of the BLMN:xMn⁴⁺ phosphors.

10 correspond to electric dipole–dipole, dipole–quadrupole and quadrupole–quadrupole interaction, respectively.⁵⁶ Fig. 5(d) shows the dependence of log(I/x) on log(x) of the BLMN:xMn⁴⁺ phosphors. The slope of the fitting line was -1.4270 . Thus $\theta = 4.281$, which was close to 3, which inferred that the concentration quenching mechanism of BLMN:Mn⁴⁺ was the non-radiative energy transfer among the adjacent Mn⁴⁺ ions.⁵⁷

The Commission International de l'Eclairage (CIE) coordinates of the BLMN:0.4% Mn⁴⁺ sample were calculated on the basis of its PL emission spectrum and the corresponding results are displayed in Fig. 6(a). The CIE chromaticity coordinates of the BLMN:0.4% Mn⁴⁺ sample were determined to be (0.7222, 0.2777) under the excitation of 360 nm. The inset shows the digital images of the as-synthesized BLMN:0.4% Mn⁴⁺ sample under daylight and 365 nm UV light. The BLMN:0.4% Mn⁴⁺ sample showed a bright far-red light. These results revealed that the BLMN:Mn⁴⁺ phosphors may be promising candidates as far-red-emitting materials for plant growth LEDs. Under 360 nm excitation, the IQE of BLMN:0.4% Mn⁴⁺ sample was measured and illustrated in Fig. 6(b). The IQE value of the BLMN:0.4% Mn⁴⁺ sample was calculated by using the following equation:⁵⁸

$$\eta = \frac{\int L_S}{\int E_R - \int E_S} \quad (4)$$

where η is IQE, L_S is the emission spectrum of the sample, E_S and E_R are the spectra of excitation light with sample and only with BaSO₄ reference, respectively. Hence, the IQE value of as-prepared BLMN:0.4% Mn⁴⁺ sample reached as high as 52%, which was higher than many recently reported Mn⁴⁺-activated red-emitting phosphors, such as SrLaScO₄:Mn⁴⁺ (IQE: 12.2%), Li₂Mg₃SnO₆:Mn⁴⁺ (IQE: 36.3%), Li₂MgZrO₄:Mn⁴⁺ (IQE: 32.3%), Ba₂YNbO₆:Mn⁴⁺ (IQE: 29.2%).^{53,51,59,60}

Fig. 7 shows the decay curves of BLMN:xMn⁴⁺ (x = 0.05%, 0.1%, 0.2%, 0.4%, 0.8%, 1.0%) phosphors monitored at 700 nm with an excitation wavelength of 360 nm. All of the decay curves were fitted with a single-exponential equation:⁶¹

$$I_t = I_0 \exp(-t/\tau) + A \quad (5)$$

where I_t and I_0 are the luminescence intensities at time t and $t = 0$, respectively; τ represents the decay time for the exponential components; and A is a constant. Based on the above equation, the lifetimes of BLMN:xMn⁴⁺ (x = 0.05%, 0.1%, 0.2%, 0.4%, 0.8%, and 1.0%) phosphors were determined to be 0.783, 0.760, 0.753, 0.733, 0.677, and 0.652 ms, respectively. As can be seen, with increasing Mn⁴⁺ doping concentrations from 0.05% to 1.0%, the lifetimes declined monotonously. This was because



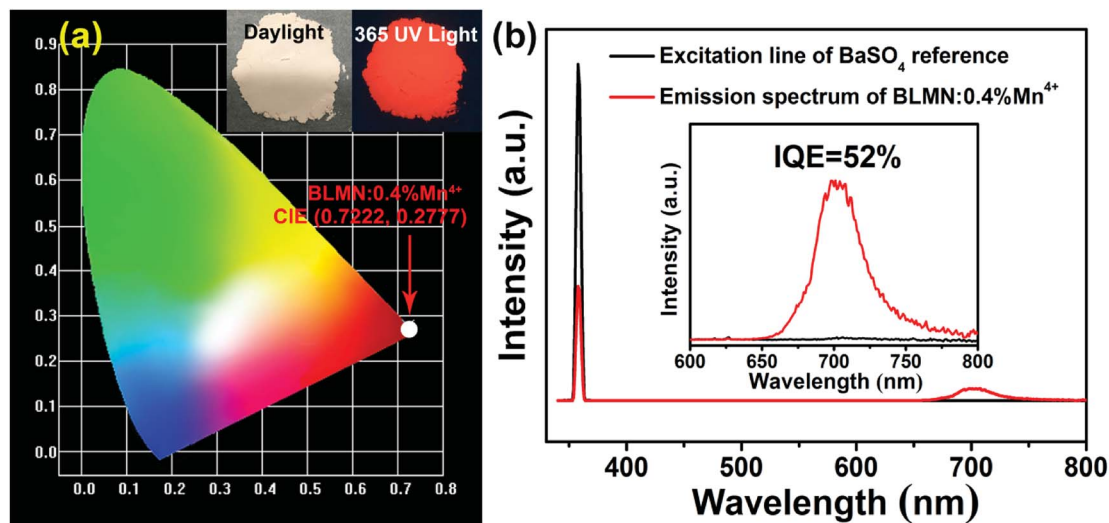


Fig. 6 (a) CIE chromaticity coordinates of BLMN:0.4% Mn⁴⁺ phosphors ($\lambda_{\text{ex}} = 360$ nm). Inset shows the digital images of BLMN:0.4% Mn⁴⁺ in daylight and under a 365 nm UV lamp. (b) Excitation line of BaSO₄ and the PL spectrum of BLMN:0.4% Mn⁴⁺ phosphor collected using an integrating sphere.

that the non-radiative energy migration among the Mn^{4+} - Mn^{4+} pairs became more faster.⁶²⁻⁶⁴

The luminescence mechanism has been analyzed by Tanabe-Sugano energy level diagram of Mn^{4+} ion in the octahedral site, as shown in Fig. 8. Mn^{4+} ion with a $3d^3$ electronic configuration belongs to transition metal ion. When excited at 375, 472, and 520 nm, the electrons at ground state ${}^4\text{A}_{2g}$ were pumped to the excited states ${}^4\text{T}_{1g}$, ${}^2\text{T}_{2g}$, and ${}^4\text{T}_{2g}$, after that the excited electrons can relax to the lowest excited state ${}^2\text{E}_g$ by non-radiative transition process. Finally, the electrons from the lowest excited state ${}^2\text{E}_g$ back to ground state may occur, thus resulting in far-red light centered at 700 nm. Crystal field intensity (Dq) can be roughly calculated using the peak energy ($19\,231\text{ cm}^{-1}$) of the ${}^4\text{A}_{2g} \rightarrow {}^4\text{T}_{2g}$ transition by the following equation:⁶⁵⁻⁶⁷

$$Dq = E(^4A_{2g} \rightarrow ^4T_{2g})/10 \quad (6)$$

thus the value of Dq was 1923 cm^{-1} . The Racah parameter B can be estimated according to the equation:⁶⁸

$$\frac{Dq}{B} = \frac{15(x-8)}{(x^2-10x)} \quad (7)$$

where x is defined as follow:⁶⁹

$$x = \frac{E(^4\text{A}_{2g} \rightarrow ^4\text{T}_{1g}) - E(^4\text{A}_{2g} \rightarrow ^4\text{T}_{2g})}{Dq} \quad (8)$$

by using the peak energy ($26\,667\text{ cm}^{-1}$) of ${}^4\text{A}_{2g} \rightarrow {}^4\text{T}_{1g}$ transition and ${}^4\text{A}_{2g} \rightarrow {}^4\text{T}_{2g}$ ($19\,231\text{ cm}^{-1}$), the value of B was then determined to be 736 cm^{-1} . Thus, Dq/B value can be calculated to be 2.61, which was beyond 2.2, indicating Mn^{4+} ions located in a strong crystal field. In additional, another Racah parameter C can be evaluated using following equation:⁷⁰

$$\frac{E(^2E_g \rightarrow ^4A_{2g})}{B} = \frac{3.05C}{B} - \frac{1.8B}{Dq} + 7.9 \quad (9)$$

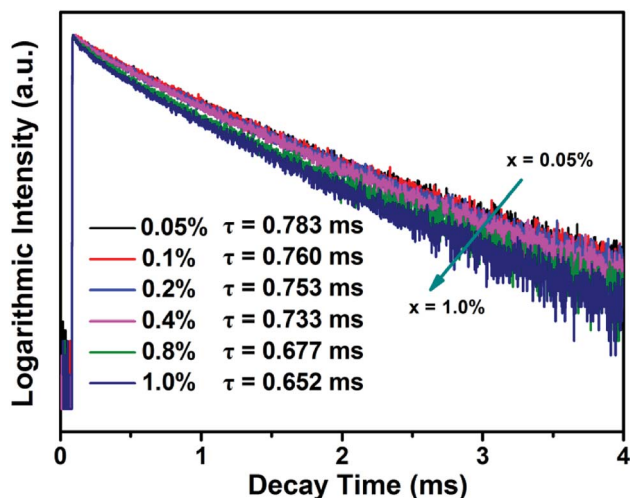


Fig. 7 Decay curves of BLMN:xMn⁴⁺ (x = 0.05%, 0.1%, 0.2%, 0.4%, 0.8%, and 1.0%) phosphors monitored at 700 nm with an excitation wavelength of 360 nm.

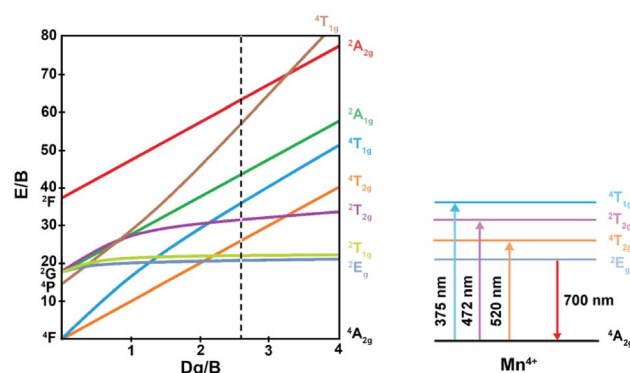


Fig. 8 Tanabe–Sugano energy-level diagram of Mn^{4+} in the octahedral site of BLMN host.

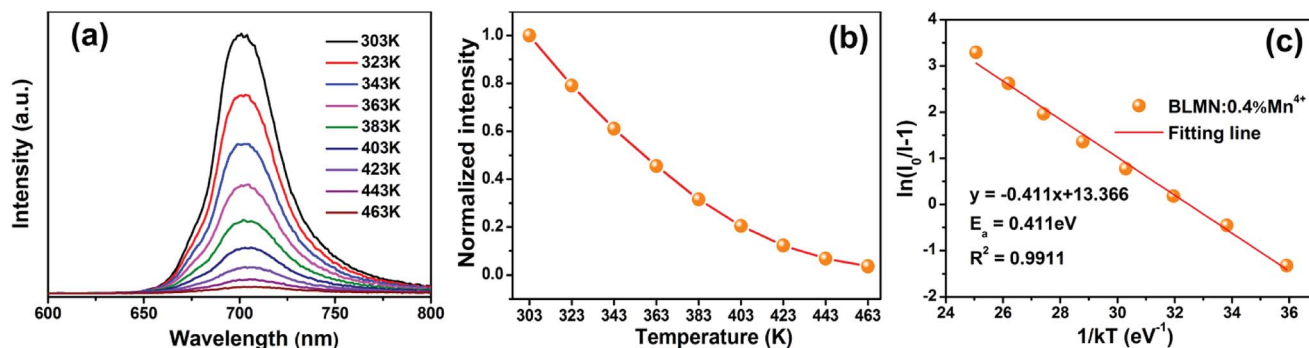


Fig. 9 (a) Temperature-dependent PL spectra of BLMN:0.4% Mn⁴⁺ phosphors under the excitation at 360 nm. (b) The dependence of the normalized emission intensity as a function of temperature. (c) Linear relationship between $\ln(I_0/I - 1)$ and $1/kT$ and the calculated activation energy (E_a) for the phosphors.

according to the peak energy ($14\,286\text{ cm}^{-1}$) of ${}^2\text{E}_g \rightarrow {}^4\text{A}_{2g}$ transition, the value for C was evaluated to be 2944 cm^{-1} .

According to the Tanabe–Sugano energy-level diagram, the wide variation in the energy of the ${}^2\text{E}_g \rightarrow {}^4\text{A}_{2g}$ transition was barely dependent on crystal field strength. It should be determined mainly by the nephelauxetic effect, which was related to the variation in the Racah parameters B and C . Brik *et al.* introduced a new parameter that described the nephelauxetic effect β_1 .^{70,71}

$$\beta_1 = \sqrt{\left(\frac{B}{B_0}\right)^2 + \left(\frac{C}{C_0}\right)^2} \quad (10)$$

where the free ion values B_0 and C_0 for the Mn⁴⁺ are 1160 cm^{-1} and 4303 cm^{-1} , respectively. B and C are the Racah parameters of Mn⁴⁺ in BLMN host. In the BLMN host the β_1 for Mn⁴⁺ was determined to be 0.93. Brik *et al.* fitted a linear relationship between the energy of the emission (${}^2\text{E}_g \rightarrow {}^4\text{A}_{2g}$ transition) and β_1 , the equation is $E({}^2\text{E}_g \rightarrow {}^4\text{A}_{2g}) = -880.49 + 16\,261.92\beta_1 \pm \sigma$, which the σ (332 cm^{-1}) represents the root-mean square (rms) deviation of the data points from the fit line.⁷² The calculated ${}^2\text{E}_g$ energy level was $13\,911\text{--}14\,575\text{ cm}^{-1}$. The experimental energy value for the ${}^2\text{E}_g \rightarrow {}^4\text{A}_{2g}$ transition of Mn⁴⁺ in the BLMN host was $14\,286\text{ cm}^{-1}$. Obviously, the result was in accord with the linear line and thus it was reliable.

Fig. 9(a) shows the temperature-dependent emission spectra of BLMN:0.4% Mn⁴⁺ phosphors in the temperature range of 303–463 K under the excitation of 360 nm. It could be observed that with increasing the temperature, the peaks shape and position were almost similar. Moreover, the normalized intensity trend of the BLMN:0.4% Mn⁴⁺ was also shown in Fig. 9(b). With increasing temperature, the PL emission intensity decreased gradually due to the temperature quenching effect. To better understand the thermal quenching characteristics, the activation energy E_a was evaluated using the following equation:²¹

$$\ln\left(\frac{I_0}{I} - 1\right) = \ln A - \frac{E_a}{kT}, \quad (11)$$

where I_0 is the initial emission intensity, I is the intensity at different temperatures, k is the Boltzmann coefficient, A is the

constant, E_a is activation energy. Linear relationship between $\ln(I_0/I - 1)$ and $1/kT$ is depicted in Fig. 9(c). The experimental data could be linear fitted with a slope of -0.411 , so the value of E_a was obtained to be 0.411 eV .

In order to further demonstrate the potential application value of the BLMN:Mn⁴⁺ phosphors in LEDs for indoor plant growth, a far-red LED device was fabricated by using as-obtained BLMN:0.4% Mn⁴⁺ phosphors coated onto a 365 nm near-UV InGaN chip. Fig. 10 shows the electroluminescent (EL) spectrum of the as-prepared LED device under the driven current of 60 mA. As shown in the inset of Fig. 10, it could be seen that the fabricated LED device clearly exhibited bright far-red light, which was attributed to a narrow emission band peaking at about 700 nm due to the ${}^2\text{E}_g \rightarrow {}^4\text{A}_{2g}$ transition of Mn⁴⁺ ions in BLMN host. The CIE chromaticity coordinates of the LED was (0.7109, 0.2890). In this work, the device has low luminous efficacy of 0.02 lm W^{-1} . Compared with plants, the ability of human eye to perceive of far red light is weaker, resulting in low luminous efficacy. These results indicated that the BLMN:Mn⁴⁺ could be considered as far-red-emitting phosphors for plant growth LEDs.

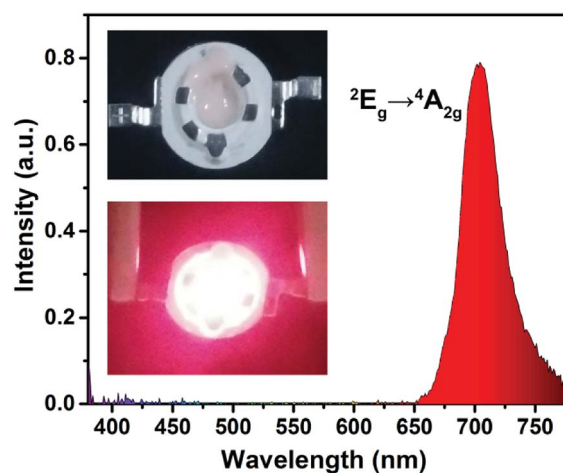


Fig. 10 EL spectrum of the fabricated far-red LED device by using BLMN:0.4% Mn⁴⁺ phosphors and a 365 nm near-UV LED chip under a current of 60 mA. Inset shows the fabricated LED device and corresponding luminescent image.



Conclusions

In summary, novel far-red-emitting BLMN:Mn⁴⁺ phosphors were successfully synthesized by the conventional high-temperature solid-state reaction method. The Rietveld refinement results indicated that the structure of sample was a cubic system in space group *Fm3m*. Monitored at 700 nm, two broad absorption bands were shown between 250 and 600 nm. With excitation of 360 and 469 nm, a far-red emission located at 700 nm within the range of 650–800 nm attributed to the ²E_g → ⁴A_{2g} transition of Mn⁴⁺ ions, which was matched well with the absorption spectra of phytochrome P_{FR}. The optimal Mn⁴⁺ doping concentration was about 0.4 mol%, and the concentration quenching mechanism of BLMN:Mn⁴⁺ was the non-radiative energy transfer among the adjacent Mn⁴⁺ ions. The CIE chromaticity coordinates and IQE of BLMN:0.4% Mn⁴⁺ sample were (0.7222, 0.2777) and 52%, respectively. In addition, the crystal field strength *Dq*, the Racah parameters *B* and *C* were calculated. The value of activation energy *E_a* was 0.411 eV. Finally, a far-red LED was fabricated by using BLMN:0.4% Mn⁴⁺ phosphors and a 365 nm near-UV LED chip. The obtained results demonstrate the BLMN:Mn⁴⁺ phosphors could be red-emitting phosphors for far-red LEDs for plant cultivation field.

Conflicts of interest

There are no conflicts to declare.

Acknowledgements

This work was supported by the National Natural Science Foundation of China (No. 51502190), the Program for the Outstanding Innovative Teams of Higher Learning Institutions of Shanxi, and the Open Fund of the State Key Laboratory of Luminescent Materials and Devices (South China University of Technology, No. 2017-skllmd-01).

Notes and references

- N. Yeh and J.-P. Chung, *Renewable Sustainable Energy Rev.*, 2009, **13**, 2175–2180.
- Z. Zhou, J. Zheng, R. Shi, N. Zhang, J. Chen, R. Zhang, H. Suo, E. M. Goldys and C. Guo, *ACS Appl. Mater. Interfaces*, 2017, **9**, 6177–6185.
- Z. Zhou, M. Xia, Y. Zhong, S. Gai, S. Huang, Y. Tian, X. Lu and N. Zhou, *J. Mater. Chem. C*, 2017, **5**, 8201–8210.
- L. Li, Y. Pan, Z. Chen, S. Huang and M. Wu, *RSC Adv.*, 2017, **7**, 14868–14875.
- R. Cao, Z. Shi, G. Quan, T. Chen, S. Guo, Z. Hu and P. Liu, *J. Lumin.*, 2017, **188**, 577–581.
- J. Long, X. Yuan, C. Ma, M. Du, X. Ma, Z. Wen, R. Ma, Y. Wang and Y. Cao, *RSC Adv.*, 2018, **8**, 1469–1476.
- J. Xiang, J. Chen, N. Zhang, H. Yao and C. Guo, *Dyes Pigm.*, 2018, **154**, 257–262.
- Y. Zheng, H. Zhang, H. Zhang, Z. Xia, Y. Liu, M. S. Molokeev and B. Lei, *J. Mater. Chem. C*, 2018, **6**, 4217–4224.
- X. Huang, H. Guo and B. Li, *J. Alloys Compd.*, 2017, **720**, 29–38.
- X. Huang, B. Li and H. Guo, *Ceram. Int.*, 2017, **43**, 10566–10571.
- P. Du, X. Huang and J. S. Yu, *Chem. Eng. J.*, 2018, **337**, 91–100.
- H. Guo, X. Huang and Y. Zeng, *J. Alloys Compd.*, 2018, **741**, 300–306.
- X. Huang, B. Li, H. Guo and D. Chen, *Dyes Pigm.*, 2017, **143**, 86–94.
- X. Huang, B. Li and H. Guo, *J. Alloys Compd.*, 2017, **695**, 2773–2780.
- X. Huang, S. Wang, B. Li, Q. Sun and H. Guo, *Opt. Lett.*, 2018, **43**, 1307–1310.
- B. Li, X. Huang, H. Guo and Y. Zeng, *Dyes Pigm.*, 2018, **150**, 67–72.
- H. Guo, B. Devakumar, B. Li and X. Huang, *Dyes Pigm.*, 2018, **151**, 81–88.
- L. Sun, B. Devakumar, B. Li, J. Liang, H. Guo and X. Huang, *RSC Adv.*, 2018, **8**, 23284–23293.
- X. Huang and H. Guo, *Dyes Pigm.*, 2018, **152**, 36–42.
- B. Li, S. Wang, Q. Sun, C. Lu, H. Guo and X. Huang, *Dyes Pigm.*, 2018, **154**, 252–256.
- H. Guo and X. Huang, *J. Alloys Compd.*, 2018, **764**, 809–814.
- B. Wang, H. Lin, J. Xu, H. Chen and Y. Wang, *ACS Appl. Mater. Interfaces*, 2014, **6**, 22905–22913.
- Y. Jin, Y. Hu, H. Wu, H. Duan, L. Chen, Y. Fu, G. Ju, Z. Mu and M. He, *Chem. Eng. J.*, 2016, **288**, 596–607.
- F. Xue, Y. Hu, L. Chen, H. Wu, G. Ju, T. Wang and L. Yang, *Ceram. Int.*, 2017, **43**, 15141–15145.
- L. Meng, L. Liang and Y. Wen, *J. Mater. Sci.: Mater. Electron.*, 2014, **25**, 2676–2681.
- H. Chen, H. Lin, Q. Huang, F. Huang, J. Xu, B. Wang, Z. Lin, J. Zhou and Y. Wang, *J. Mater. Chem. C*, 2016, **4**, 2374–2381.
- Y. Zhu, L. Cao, M. G. Brik, X. Zhang, L. Huang, T. Xuan and J. Wang, *J. Mater. Chem. C*, 2017, **5**, 6420–6426.
- L. Huang, Y. Liu, J. Yu, Y. Zhu, F. Pan, T. Xuan, M. G. Brik, C. Wang and J. Wang, *ACS Appl. Mater. Interfaces*, 2018, **10**, 18082–18092.
- M. Zhu, Y. Pan, L. Xi, H. Lian and J. Lin, *J. Mater. Chem. C*, 2017, **5**, 10241–10250.
- M. Zhu, Y. Pan, Y. Huang, H. Lian and J. Lin, *J. Mater. Chem. C*, 2018, **6**, 491–499.
- A. Fu, Q. Pang, H. Yang and L. Zhou, *Opt. Mater.*, 2017, **70**, 144–152.
- G. Jiang, B. Yang, G. Zhao, Y. Liu, J. Zou, H. Sun, H. Ou, Y. Fang and J. Hou, *Opt. Mater.*, 2018, **83**, 93–98.
- J. Zhong, D. Chen, X. Chen, K. Wang, X. Li, Y. Zhu and Z. Ji, *Dalton Trans.*, 2018, **47**, 6528–6537.
- J. Zhong, S. Zhou, D. Chen, J. Li, Y. Zhu, X. Li, L. Chen and Z. Ji, *Dalton Trans.*, 2018, **47**, 8248–8256.
- L. Li, W. Chang, W. Chen, Z. Feng, C. Zhao, P. Jiang, Y. Wang, X. Zhou and A. Suchocki, *Ceram. Int.*, 2017, **43**, 2720–2729.
- X. Huang, J. Liang, B. Li, L. Sun and J. Lin, *Opt. Lett.*, 2018, **43**, 3305–3308.
- J. Liang, L. Sun, B. Devakumar, S. Wang, Q. Sun, H. Guo, B. Li and X. Huang, *RSC Adv.*, 2018, **8**, 27144–27151.



- 38 X. Huang, *J. Alloys Compd.*, 2017, **690**, 356–359.
- 39 P. Du, L. Luo, X. Huang and J. S. Yu, *J. Colloid Interface Sci.*, 2018, **514**, 172–181.
- 40 P. Du, X. Huang and J. S. Yu, *Inorg. Chem. Front.*, 2017, **4**, 1987–1995.
- 41 Z. Lu, T. Huang, R. Deng, H. Wang, L. Wen, M. Huang, L. Zhou and C. Yao, *Superlattices Microstruct.*, 2018, **117**, 476–487.
- 42 A. Fu, C. Zhou, Q. Chen, Z. Lu, T. Huang, H. Wang and L. Zhou, *Ceram. Int.*, 2017, **43**, 6353–6362.
- 43 A. Fu, A. Guan, D. Yu, S. Xia, F. Gao, X. Zhang, L. Zhou, Y. Li and R. Li, *Mater. Res. Bull.*, 2017, **88**, 258–265.
- 44 K. Li, H. Lian and R. V. Deun, *J. Lumin.*, 2018, **198**, 155–162.
- 45 B. Li and X. Huang, *Ceram. Int.*, 2018, **44**, 4915–4923.
- 46 Q. Sun, S. Wang, B. Li, H. Guo and X. Huang, *J. Lumin.*, 2018, **203**, 371–375.
- 47 Q. Peng, R. Cao, Y. Ye, S. Guo, Z. Hu, T. Chen and G. Zheng, *J. Alloys Compd.*, 2017, **725**, 139–144.
- 48 C. Yang, Z. Zhang, G. Hu, R. Cao, X. Liang and W. Xiang, *J. Alloys Compd.*, 2017, **694**, 1201–1208.
- 49 S. Liang, M. Shang, H. Lian, K. Li, Y. Zhang and J. Lin, *J. Mater. Chem. C*, 2016, **4**, 6409–6416.
- 50 S. Liang, M. Shang, H. Lian, K. Li, Y. Zhang and J. Lin, *J. Mater. Chem. C*, 2017, **5**, 2927–2935.
- 51 R. Cao, Z. Shi, G. Quan, Z. Luo, P. Tang, H. Ao and X. Yu, *Opt. Mater.*, 2016, **57**, 212–216.
- 52 R. Cao, X. Liu, K. Bai, T. Chen, S. Guo, Z. Hu, F. Xiao and Z. Luo, *J. Lumin.*, 2018, **197**, 169–174.
- 53 R. Cao, X. Ceng, J. Huang, H. Ao, G. Zheng, X. Yu and X. Zhang, *Opt. Mater.*, 2016, **62**, 706–710.
- 54 G. Blasse, *Phys. Lett. A*, 1968, **28**, 444–445.
- 55 D. L. Dexter, *J. Chem. Phys.*, 1953, **21**, 836–850.
- 56 J. He, X. Guo, Y. Chen, R. Shi, Y. Huang, J. Zhang, Y. Wang and Z. Liu, *Chem.–Eur. J.*, 2018, **24**, 1287–1294.
- 57 Q. Shao, H. Ding, L. Yao, J. Xu, C. Liang and J. Jiang, *RSC Adv.*, 2018, **8**, 12035–12042.
- 58 X. Huang and H. Guo, *Dyes Pigm.*, 2018, **154**, 82–86.
- 59 U. B. Humayoun, S. N. Tiruneh and D.-H. Yoon, *Dyes Pigm.*, 2018, **152**, 127–130.
- 60 R. Cao, J. Zhang, W. Wang, Z. Hu, T. Chen, Y. Ye and X. Yu, *Mater. Res. Bull.*, 2017, **87**, 109–113.
- 61 R. Cao, X. Ceng, J. Huang, X. Xia, S. Guo and J. Fu, *Ceram. Int.*, 2016, **42**, 16817–16821.
- 62 X. Ding, Q. Wang and Y. Wang, *Phys. Chem. Chem. Phys.*, 2016, **18**, 8088–8097.
- 63 S. Zhang, Y. Hu, H. Duan, L. Chen, Y. Fu, G. Ju, T. Wang and M. He, *RSC Adv.*, 2015, **5**, 90499–90507.
- 64 G. Hu, X. Hu, W. Chen, Y. Cheng, Z. Liu, Y. Zhang, X. Liang and W. Xiang, *Mater. Res. Bull.*, 2017, **95**, 277–284.
- 65 B. Wang, H. Lin, F. Huang, J. Xu, H. Chen, Z. Lin and Y. Wang, *Chem. Mater.*, 2016, **28**, 3515–3524.
- 66 X. Zhang, J. Nie, S. Liu, Y. Li and J. Qiu, *J. Am. Ceram. Soc.*, 2017, **101**, 1576–1584.
- 67 S. Zhang, Y. Hu, H. Duan, Y. Fu and M. He, *J. Alloys Compd.*, 2017, **693**, 315–325.
- 68 S. Zhang and Y. Hu, *J. Lumin.*, 2016, **177**, 394–401.
- 69 W. Chen, Y. Cheng, L. Shen, C. Shen, X. Liang and W. Xiang, *J. Alloys Compd.*, 2018, **762**, 688–696.
- 70 M. G. Brik, S. J. Camardello, A. M. Srivastava, N. M. Avram and A. Suchocki, *ECS J. Solid State Sci. Technol.*, 2016, **5**, R3067–R3077.
- 71 Y. Chen, K. Wu, J. He, Z. Tang, J. Shi, Y. Xu and Z. Liu, *J. Mater. Chem. C*, 2017, **5**, 8828–8835.
- 72 M. G. Brik, S. J. Camardello and A. M. Srivastava, *ECS J. Solid State Sci. Technol.*, 2015, **4**, R39–R43.

